A combined experimental and modeling study revealing the anisotropic mechanical response of Ti_2AlN MAX phase

Xiaoqiang Li [a,*], Jürgen Malzbender [a], Gang Yan [a], Jesus Gonzalez-Julian [a], Ruth Schwaiger [a, b]

[a] Forschungszentrum Jülich GmbH, Institute of Energy and Climate Research, 52425 Jülich, Germany

[b] Chair of Energy Engineering Materials, RWTH Aachen University, 52056 Aachen, Germany

Corresponding author*: xi.li@fz-juelich.de

Abstract

Ti_2AlN MAX phase with a hexagonal crystal structure exhibits great potential as structural material for operation under harsh environments due to its excellent mechanical performance. For a reliable application, a comprehensive understanding of the mechanical behavior, and in particular of the anisotropic properties is needed. Thus, in this study, we combined nanoindentation and electron-backscatter diffraction experiments to correlate elastic modulus and hardness of Ti_2AlN to the crystallographic orientation. We used two different modeling approaches to better understand, validate, and in the long run to predict the anisotropic mechanical behavior of MAX phase materials. While we observed consistent trends in both experiments and modeling, elastic modulus and hardness showed different dependencies on the crystal orientation.

Keywords: MAX phases; anisotropy; nano-indentation; EBSD; mechanical properties;

1. **Introduction**

In the year 2000, the "$M_{n+1}AX_n$" ceramics were initially reported by Barsoum et al. [1], defined as ternary carbides and nitrides, where "M" is an early transition element, A represents elements of group IIIA to VIA and "X" corresponds to either C or N [2-3]. Currently, more than 150 different MAX phase materials have been discovered and all of them possess a hexagonal crystal structure, where alternating near-close-packed layers of M_6X octahedral interleave with A-A layers [4]. This unique crystal structure combines metallic and covalent/ionic bonding [5], resulting in properties that are typical of ceramics, such as low density, high elastic modulus, and excellent oxidation and corrosion resistance at high temperature [4], as well as characteristics typical of metals, such as high electrical and thermal conductivities, good thermal shock resistance and damage tolerance, and easy machinability [4].

Considering the attractive properties listed above, MAX phase materials are promising candidates as structural materials for applications which expose them to aggressive environments, due to the excellent mechanical performance at ambient and high temperatures, as well as their good oxidation and corrosion resistance [3-4]. In particular, Ti_2AlN, one member of aluminum-based MAX phase ceramics, exhibits an excellent combination of such properties for high temperature applications [5-6]. Currently, bulk Ti_2AlN ceramics are widely investigated, which are mainly fabricated via hot pressing [7-11], spark plasma sintering [12-14], hot isostatic pressing [15], shock-activated reaction synthesis [16] and microwave sintering [17] on the basis of Ti/Al/TiN or Ti/AlN powder mixtures.

MAX phases are usually consolidated as polycrystalline bulk material or thin film, and usually the anisotropic structure can be preserved only at a microscopic level [18]. However, single crystals are required to characterize the full anisotropy of the compounds [18]. Single-crystalline phases have been obtained either by thin layer heteroepitaxy [19-21], bulk crystal growth or as textured epilayers [19, 22-24]. In addition, various single crystals were synthesized, such as single crystalline platelets of Cr_2AlC with typical areas in the range of a few mm^2 [18], and single crystals of Ta_4AlC_3 and Ta_3AlC_2 with lateral dimensions of 0.02 mm, thickness of 0.005 mm, i.e. a volume of $0.02 \times 0.02 \times 0.005\ mm^{3.}$ [22]. Ti_3SiC_2 single crystals were obtained with dimensions of a few hundred microns thick and several millimeters in length and width [23-24]. The preparation methods exhibit some limitations, including complexity of the processing, high cost, and rather small dimensions.

Regarding the textured MAX phases, more information is already available, and more compositions have been processed. Ti_3SiC_2 presented inhomogeneous texturing [25], while better results have been obtained for Nb_4AlC_3 with a Lotgering orientation factor $f(00l)$ of approximately 1 on textured top surfaces [26-

28], Ti_3AlC_2 and Ti_2AlC with texturing degree $f(00l)$ on textured top surfaces of 0.51 and 0.49, respectively [29]. Higher Lotgering orientation factors $f(00l)$ of Ti_2AlC and Ti_3AlC_2 were achieved, i.e. 0.82 and 0.71 respectively, via a two-step hot pressing procedure [30]. Ti_2AlN with Lotgering orientation factor $f(00l)$ on textured top surfaces of 0.8 [31], and Cr_2AlC with low texturing degree [32] were synthesized. Especially Ti_2AlN is a very suitable representative of the MAX phase family, allowing the investigation of the mechanical performance and potential effects of the crystallographic orientation.

Recently, the deformation behavior of micron-sized single-crystal Ti_2InC and Ti_4AlN_3 specimens has been investigated under uniaxial compression [33]. It was observed that deformation behavior was associated with the slip on single planes or sets of parallel planes. Moreover, the direct observation of nucleation and propagation of basal plane dislocations within Nb_2AlC using nanomechanical testing inside a transmission electron microscope was reported [34], the different loading directions with respect to the basal plane contributed to a completely different plastic response due to the pronounced anisotropy of the layered crystal. Furthermore, the anisotropic deformation of Ti_3SiC_2 single crystals has been investigated at room temperature as a function of loading axis orientation and specimen size by microcompression tests [35], where the basal slip appeared to be the operative slip system at room temperature.

Often nanoindentation testing is used for characterization of elastic modulus and hardness of materials [36]. This technique offers several advantages, including the need for only small samples, straightforward sample preparation since only a flat well-polished surface is needed, well-defined test procedures, and easy handling of instrumentation [37-40]. Indentation experiments are often applied to characterize single grains and textured or single crystal epitaxial thin films [41]. Often it is assumed that for such anisotropic materials the elastic modulus is a polycrystalline average of the elastic constants or corresponds to the elastic modulus in the direction of the indentation [41]. However, the indentation process induces a half-spherical deformation field, making it difficult to determine the properties for a particular direction. Only apparent properties are derived that are a representation of the deformation field.

Some previous works concentrated on comparisons of experimental results with data derived from analytical and numerical approaches. For example, experimental stress–strain curves and crystallographic texture evolution effects for an initially-textured polycrystalline magnesium alloy AZ31B were compared to a crystal-mechanics-based model regarding the inelastic deformation of HCP metals deforming by slip and twinning via an implementation into the finite-element program ABAQUS [42], furthermore, the behavior of single crystal Mg, α-Ti-7 wt.% Al alloy and single crystal 6H-SiC was compared to simulations using anisotropic elastic contact theory and Hertzian contact mechanics [43-45], the behavior of textured $KSr_2Sb_5O_{15}$ ceramics was compared to ab-initio calculations [46], austenitic stainless steel (grade A304) to

finite element simulations [47], the behavior of polycrystalline ZrB_2 [48] and Al_2O_3 [49], $Li_{1.3}Al_{0.3}Ti_{1.7}(PO_4)_3$ [50], WC [51] and β-Si_3N_4 [52] was studied using the Vlassak-Nix and easy-slip models [49-50, 53-54]. The Vlassak-Nix model [41] was shown to predict the indentation elastic modulus of anisotropic solids such as brass and copper, and was later successfully applied to characterize a number of different materials [48-52, 55-57]. The easy-slip model was introduced by Csanádi et al [51-52] to calculate the hardness-orientation dependency of WC material [51] and the influence of crystal orientation on nano hardness and indentation modulus of grains in polycrystalline β-Si_3N_4 [52]. The calculated results were in good agreement with experimental results. Although it is not possible to predict the exact value of a material's hardness, the variation of the relative hardness determined still reveals the dependence on the orientation. In order to investigate the anisotropic mechanical properties of the MAX phase, nano-indentation and EBSD analyses were combined to study the correlations of elastic modulus and hardness with the crystal orientation.

The aim of this work is to investigate the anisotropy of the mechanical properties of Ti_2AlN phase. The experimentally derived elastic modulus and hardness of Ti_2AlN are presented to gain insight into orientation effects. The results are compared with the data derived from the Vlassak-Nix and easy-slip models.

2. Experimental procedure

2.1 Fabrication of polycrystalline Ti_2AlN material via FAST/SPS

The fabrication process of bulk Ti_2AlN has been reported in detail elsewhere [12]. Briefly, titanium (-325 mesh, 99.5% pure), aluminum (-325 mesh, 99.5% pure) and titanium nitride (-325 mesh, 99.5% pure) powders (all from Alfa Aesar, Germany) were used as starting precursors. The powders were weighted according to the formula of Ti: 1.02Al: TiN, and mixed using a roller bench with ethanol as liquid media for 24 h at 250 r.p.m. After the ball mixing, the slurry was dried at 60 °C in air for 2 days.

Dense and highly pure bulk Ti_2AlN samples were sintered via Field Assisted Sintering Technology/Spark plasma sintering (FAST/SPS) (FCT-HPD5, FCT Systeme GmbH, Germany). The mixed powder was first heated up at 20 K/min and a uniaxial pressure of 20 MPa up to 1000 °C, followed by a heating rate of 50 K/min and a pressure of 40 MPa up to the maximal temperature 1400 °C, with a dwell time of 30 min. The as-obtained bulk Ti_2AlN samples were cut and embedded in water-free epoxy resin, then ground with 400-4000-grid SiC sandpapers and polished with 3 μm and subsequently 1 μm diamond polishing paste (Diamond Polishing Compound, MetaDi, BUEHLER, USA) followed by colloidal silica suspension (50 nm Alkaline, CLOEREN TECGNOLOGY GmbH).

The densities were measured applying the Archimedes principle in water at room temperature. The phase compositions and the amount of different phases within the bulk materials were identified by X-ray

Diffraction (XRD, D8-Discover, Bruker, US) and Rietveld refinement on the polished surfaces. The microstructures were characterized via field emission scanning electron microscopy (SEM, Merlin, Zeiss Microscopy, Oberkochen, Germany). In addition, electron backscatter diffraction (EBSD, Oxford NordlysNano) was employed to characterize grain sizes and crystal orientations of the obtained Ti_2AlN samples and the surface topography of the imprint was studied by atomic force microscopy (AFM, Dimension Icon, Bruker, Santa Barbara, USA).

2.2 Nanoindentation

The indentation tests were conducted at room temperature using a NanoTest Xtreme test setup from Micro Materials® (Wrexham, UK) equipped with a diamond Berkovich tip. The samples were indented at constant load rate of 2.5 mN/s to maximum depth of 300 nm. When the maximum depth was reached, the load was held constant for 10 s before unloading the sample. The analysis of the data was based on an automatic procedure of the instrument following the Oliver-Pharr methodology [36] and ASTM E2546-07 [53]. Modulus and hardness were derived from the load-displacement data via the determination of contact stiffness from the unloading portion, yielding apparent properties for the anisotropic materials that require further comparison with modelled data and deconvolution. Poisson's ratio and Young's modulus of diamond were assumed as $\nu_i = 0.07$ and $E_i = 1141$ GPa, respectively. Considering the assumed anisotropic nature of Ti_2AlN MAX phase material, the apparent properties termed indentation modulus (M) representing the elastic behavior of the anisotropic material was derived from the reduced indentation modulus data (E_r), M is determined from [41]:

$$\frac{1}{M} = \frac{1}{E_r} - \frac{1-\upsilon_i{}^2}{E_i}$$

In addition, indentation hardness as another apparent property, was also obtained [36, 53].

$$H = \frac{P_{max}}{A_p}$$

Where P_{max} is the peak indentation load and A_p is the projected area of the indent.

After nano indentation testing, the orientations of the indented grains were characterized by EBSD. Due to the test limitation of the indenter (allowing a maximum of 400 indents per test set), four individual arrays were prepared. The distance between the indents was fixed to 8 μm to avoid interaction of the stress fields of neighboring indents. When establishing the dependence of indentation results on grain orientation, only indents inside Ti_2AlN grains were considered, while indents close to a grain boundary were not taken into account. Only grains with at least three indents were considered for further analysis.

The orientation of the Ti_2AlN grains was analyzed using the open source MATLAB toolbox MTEX [54]. In the EBSD analysis, the Bunge Euler angles (ϕ_1, Φ, ϕ_2) are used to describe the grain orientation. As Ti_2AlN has a hexagonal structure, only Φ and ϕ_2 angles were considered as the relevant indices to determine the possible effect of orientation on the elastic modulus and hardness. The three angles are theoretically in the range of [0, 2π]. According to the hexagonal symmetry, Φ is in the range of [0, $\pi/2$], while ϕ_2 is in the range of [0, $\pi/3$]. In this work, the angle Φ is the angle of crystal rotation from the parallel of the basal (0001) orientation plane to the vertical of the basal plane. The angle ϕ_2 represents the angle of the indented plane rotating from the prismatic $(10\bar{1}0)$ type plane to another $(10\bar{1}0)$ plane through the prismatic $(11\bar{2}0)$ type plane.

2.3 Prediction of elastic modulus and hardness

The Vlassak-Nix and easy-slip models were adopted for comparison with the experimental results to understand the mechanical anisotropy of Ti_2AlN material.

An assumption is about the slip systems of the Ti_2AlN material for both models, which is different in this work compared to that of WC reported in [51]. Because of the layered nature of the crystal structure as well as the very high *c*/*a* ratios, MAX phase compounds are predicted to exhibit strong anisotropy in the plastic deformation and fracture behavior [58-66]. Previous experimental studies have indicated that polycrystals of the MAX phase compounds such as Ti_3SiC_2 and Ti_2AlN deform by the predominant activation of basal slip, kink band formation and delamination along basal planes [58-64], while a predominant activation of basal slip is usually observed in HCP metals with a relatively large *c*/*a* ratio [65-66].

In order to simplify the Vlassak-Nix model, the contact area is converted to a circular area, which leads to the calculation of the indentation modulus M as shown in equation (1). The h_0 here is the first term in the Fourier series representation of function $h(\theta)$ related to θ, which is demonstrated in equation (2). Here θ is the angle representing the direction variation of point load in a specific surface ranged in [0, π]. The α_i represents the direction cosines of the angle between the load direction and the crystal coordinate system axes. Equation (3) and equation (4) are the expansion form of equation (2) and equation (3), respectively. Regarding equation (3), one right-hand Cartesian coordinate $(\vec{m}, \vec{n}, \vec{t})$ is built where the $\vec{t}$ axis was vertical to the load direction, in which ϕ is the angle between vector $\vec{m}$ and a fixed vector in the $(\vec{m}, \vec{n})$ plane. The C_{ijkm} in equation (4) contains the elastic parameters of the anisotropic material based on the elastic constants of the material. The relationship between the parameters C_{ijkm} and the elastic constants C_{pq} are as follows:

the tensors *ij* (or *km*) are reflected on the tensor *p* (or *q*) as 11 → 1, 22 → 2, 33 → 3, 23 and 32 → 4, 13 and 31 → 5, 21 and 12 → 6.

$$M = \frac{1}{\pi h_0} \tag{1}$$

$$h(\theta) = \frac{1}{8\pi^2}(\alpha_k B_{km}^{-1} \alpha_m) \tag{2}$$

$$B_{js}(\mathbf{t}) = B_{sj}(\mathbf{t}) = \frac{1}{8\pi^2}\int_0^{2\pi}\{(\mathbf{mm}\}_{js} - (\mathbf{mn})_{jk}(\mathbf{nn})_{kr}^{-1}(\mathbf{nm})_{rs}\}\mathrm{d}\phi \tag{3}$$

$$(\mathbf{ab})_{jk} = a_i C_{ijkm} b_m \tag{4}$$

$$C_{pq} = \begin{pmatrix} 311 & 71 & 102 & 0 & 0 & 0 \\ 71 & 305 & 102 & 0 & 0 & 0 \\ 102 & 102 & 298 & 0 & 0 & 0 \\ 0 & 0 & 0 & 133 & 0 & 0 \\ 0 & 0 & 0 & 0 & 133 & 0 \\ 0 & 0 & 0 & 0 & 0 & 120 \end{pmatrix} \tag{5}$$

Here, the elastic constants of Ti_2AlN reported in [67] with the unit GPa as given in equation (5), were employed in the Vlassak-Nix model. Taking the symmetry of the hexagonal structure into consideration in the Vlassak-Nix model, the angle Φ from basal plane to the perpendicular direction with 1° per step, and for different angles of ϕ_2 in the basal plane, were adopted to calculate the orientation dependency of the indentation modulus.

The "easy-slip" model, which has been adopted here to predict the hardness variation related to the orientation of the anisotropic material, is based on the assumption that the stress distribution confined in the indentation area is uniform, i.e., the stress component surrounding the indenter is compressive and perpendicular to the indenter profile [51-52].The hardness can be calculated via equation (6). A conical rigid indenter with a semi-angle γ of 65° was used in the model to simplify the calculation and ensure comparability with the Vlassak-Nix model. Additionally, friction during indentation is neglected. Another assumption is that just one dislocation slip system family is operative contributing to the plastic deformation. Slip can only occur when the shear stress reaches a critical value for a specific direction, which results in the name of "easy-slip". Here, the Schmid factor for calculating the normal stress, as illustrated in our previous work [50], is introduced in equation (7), assuming that the critical resolved shear stress is constant. The calculation of normal stress follows equation (8).

In total six slip systems are first considered in the easy slip model with $\overrightarrow{n_i}$ as the normal vector for the slip plane and $\overrightarrow{v_{ij}}$ as the slip direction vector as illustrated in previous work [50]: $\overrightarrow{n_0}$ = (0001): $\overrightarrow{v_{01}}$ = $[11\bar{\bar{2}}0]$, $\overrightarrow{v_{02}}$ = $[2\bar{1}\bar{1}0]$, $\overrightarrow{v_{03}}$ = $[\bar{1}2\bar{1}0]$, $\overrightarrow{n_1}$ = $(11\bar{2}0)$: $\overrightarrow{v_{11}}$ = $[1\bar{1}00]$, $\overrightarrow{n_2}$ = $(\bar{1}2\bar{1}0)$: $\overrightarrow{v_{21}}$ = $[10\bar{1}0]$, $\overrightarrow{n_3}$ = $(2\bar{1}\bar{1}0)$:

$\overrightarrow{v_{31}} = [01\bar{1}0]$. The vectors $\overrightarrow{n_i}$ and $\overrightarrow{v_{ij}}$ should be normalized during calculation. In the current study, only $\overrightarrow{n_0}$, $\overrightarrow{v_{01}}$, $\overrightarrow{v_{02}}$ and $\overrightarrow{v_{03}}$ were considered based on the predominant slip systems discussed in the introduction section for Ti_2AlN materials. The glide systems are $\{0001\}<11\bar{2}0>$ in basal plane, whereas the slip in prismatic and pyramidal planes are out of consideration based on the arguments presented above. Similar to the previous work [50], an improvement of the original model is made according to [52], i.e. the average of the maximum Schmid factor at the specific rotation angle Φ is considered rather than the maximum Schmid factor directly as shown in equation (9). With these assumptions, the relation between the hardness and the orientation of the Ti_2AlN material can be expressed as a ratio of the hardness for a specific plane and the hardness for the prismatic plane as demonstrated in equation (10), which is equal to the inverse ratio of the corresponding average maximum Schmid factor.

$$H = \frac{F}{A} = \frac{\sigma \times A_c}{A} \tag{6}$$

$$\tau = \frac{dF \times \cos\alpha}{dA'} = \frac{dF \times \cos\alpha}{\frac{dA}{\cos\beta}} = \frac{dF}{dA} \times \cos\alpha \times \cos\beta = \sigma \times \cos\alpha \times \cos\beta = \sigma \times m(\phi) \tag{7}$$

$$\sigma = \left(\frac{\tau}{m(\phi)}\right)_{min} = \frac{\tau_{CRSS}}{(m(\phi))_{avg,max,\phi}} \tag{8}$$

$$m(\phi)_{avg,max,\phi}(\Phi) = \frac{1}{2\pi}\int_0^{2\pi} \max_{i,j}\left(m_{i,j}(\Phi,\phi)\right) d\phi \tag{9}$$

$$\frac{H(\Phi)}{H_{prismatic}} = \frac{H(\Phi)}{H(\Phi = 90^\circ)} = \frac{m_{avg,max,\phi}(\Phi = 90^\circ, \phi)}{m_{avg,max,\phi}(\Phi,\phi)} \tag{10}$$

Where F, A, A_c, σ are applied load, projected area, contact area and the compression stress acting on the cone surface, respectively. τ,τ_{CRSS}, dF, dA, dA', m, $m_{avg,max}$, α and β present the local shear stresses, the critical shear stress, the elementary force, elementary area, elementary area of the slip plane, the Schmid factor, the average of the maximum Schmid factor, the angles between the slip direction, the slip plane normal vectors and the elementary force vector, respectively.

3. Results and Discussion

3.1 Microstructure and orientation distribution

Fig. 1 presents the XRD pattern of the sintered sample with all diffraction peaks corresponding to Ti_2AlN. The amount of different phases and the lattice parameters, which were also derived by Rietveld refinement,

are summarized in Table 1. Based on the Rietveld refinement, the as-obtained Ti_2AlN specimen has no detectable impurities, similar as reported in previous work [12], confirming the high purity of the material.

The lattice parameters of Ti_2AlN, calculated from the Rietveld refinement, are $a^* = b^* = 2.987$ Å, $c^* = 13.645$ Å, and in good agreement with the values reported in literature [3, 13]. The Ti_2AlN samples have a density of 4.30 ± 0.01 g/cm^3 (theoretical density is 4.31 g/cm^3 [3, 13]), yielding a porosity of less than 1%. SEM images of a polished surface and a fracture surface are displayed in Fig. 2. It is clear from Fig. 2(a) that the material is almost fully dense. In addition the typical nano-laminated microstructure of the MAX phase ceramics is presented in Fig. 2(b).

In order to characterize the grain distribution, the phase and orientation mappings are given in Fig. 3. As shown in Fig. 3(a), the red phase corresponds to Ti_2AlN grains, while the yellow phase represents traces of Al_2O_3. Based on the EBSD technique, the area ratios of Ti_2AlN and Al_2O_3 presented in Table 1 are 99.7 % and 0.3 %, respectively, which fits well with the purity calculated via Rietveld refinement above although slight difference on the purity of the as-obtained Ti_2AlN material due to the detection accuracy for XRD characterization. In addition, the grain size of Ti_2AlN was determined as 13 ± 7 μm via EBSD.

The Lotgering orientation factor $f(l)$ [27, 30] was determined as follows: $f(l) = (P - P_0)/(1 - P_0)$. For *c*-axis orientation, P and P_0 were obtained from the ratio of $\sum(00l)/\sum(hkl)$. Here, P corresponds to the textured Ti_2AlN sample and P_0 was obtained from the XRD data (PDF card No: 18-0070). $\sum(00l)$ and $\sum(hkl)$ were the sums of peak intensities corresponding to the $(00l)$ and (hkl) planes, respectively. The Lotgering orientation factor$f(00l)$for the top surfaces of the obtained Ti_2AlN specimen was calculated to be as low as 0.07. Furthermore, the orientation of the phases of Ti_2AlN grains shown in Fig. 3(b-d) clearly reveals that the Ti_2AlN grains are orientated highly randomly. Therefore, it is possible to obtain sufficient mechanical data for different orientations from the sample, which has no obvious texture.

The areas that were chosen for nano-indentation testing are presented in Fig. 4(a). Typical morphologies of imprints at different magnifications are displayed in Fig. 4(b) and Fig. 4(c). It can be seen in Fig. 4(a) that the indentations are homogeneously distributed across the polished surface. The distance between the indents was fixed at 8 μm. No obvious interaction between the imprints inside the grain is visible in Fig. 4(b-c), which manifests that the indentations represent a local property of each individual Ti_2AlN grain. Moreover, as presented in the Fig. 4 (d), the additional AFM image and corresponding line scan did not reveal any pronounced effect of pile-up, hence, overall, the Oliver-Pharr approach that was used to analyze the data appears to be appropriate.

As illustrated in Fig. 5(a), some of the imprints are close to grain boundaries. In the further analysis, only imprints having a regular shape and at sufficient distance from grain boundaries were considered. The orientation mapping of the indentation matrix is shown in Fig. 5(b-c).

3.2 Mechanical properties

Typical indentation load-depth curves for the three specific planes are presented in Fig. 6. The specific planes are illustrated in Fig. 6 (a). Figure 6(b) shows the curves of an indent into the basal plane and the prismatic $(10\bar{1}0)$ and $(11\bar{2}0)$ planes. In addition, no obvious creep behavior was observed during the dwelling time as presented in Fig. 6(c). The shape of the curves is different for the three planes, which indicates anisotropic mechanical properties. As expected, the maximum loads for the two prismatic planes are very similar, whereas the maximum load for the basal plane is much higher.

The indentation modulus (M) and hardness (H) of the Ti_2AlN sample are shown in Fig. 7 with the two axes representing the angle from the basal orientation (Φ) and the angle from prismatic orientation (ϕ_2). Here the surface mapping has no physical meaning and is only used to guide the eye and point out the dependency of the mechanical properties on the rotation angles. To permit a deeper understanding of the graphs the deviations of M and H are shown and discussed in more detail below.

It can be seen in Fig. 7(a-b) that indentation modulus and hardness of Ti_2AlN show a different trends regarding the variation of the angles from the basal plane Φ and the prismatic plane ϕ_2. Note that, with increasing of Φ describing the angle of the indented plane rotating from the basal plane towards the prismatic plane, the value of M first increased from ~296 to ~308 GPa for the angle ranging from 1 to 30° then decreased dramatically to ~239 GPa at the angle of 90°. The hardness changes slightly, first decreasing from 15 GPa to 11 GPa with Φ ranging from 0° to 43°, then slightly increasing to 12 GPa at 90°, as shown in Fig. 7(a-b). In order to gain clearer observation of the tendency of the values, corresponding 2D color-maps of the data were presented in Fig. 7(c-d), for ϕ_2, which is the angle of the indented plane rotating from the prismatic $(10\bar{1}0)$ type plane to another $(10\bar{1}0)$ plane through the prismatic $(11\bar{2}0)$ type plane, the indentation moduli and hardness are almost constant considering the measurement uncertainty. Hence, ϕ_2 has no effect on the mechanical response. Therefore, the rotation angle Φ is the predominant factor influencing the anisotropic behavior of the Ti_2AlN material, which agrees well with results reported for $Li_{1.3}Al_{0.3}Ti_{1.7}(PO_4)_3$ (LATP) ceramic electrolyte with a rhombohedral crystal structure [50] and the hexagonal material β-Si_3N_4 [52].

As mentioned above, the Vlassak-Nix and easy-slip models were adopted to calculate indentation modulus (M) and hardness ratio (normalized H using a reference value of the hardness at Φ = 90°), respectively, for

the rotation angles of the crystal structure, as shown in Fig. 8. The indentation modulus and hardness ratio are derived as a function of Φ from 0° to 180° with 1° per step to further illustrate the variation. In order to illustrate the effects on the mechanical properties with respect to angle ϕ_2, i.e., the angle for calculation between the normal of the indented surface and the X-Z plane of the crystal coordinate system at X-Y plane, typical plots at ϕ_2 = -30°, 0° and 30°, are selected for the calculation of both indentation modulus and hardness ratio.

Regarding Φ ranging from 0° to 90°, i.e. the indented plane being rotated from the basal plane to the prismatic plane, the indentation modulus first increases from 0° to 37° followed by a continuous decrease with a maximum value of ~303 GPa at 37° and a minimum value of ~290 GPa at 90°. With respect to the hardness ratio, values for the hardness at 90° are used as a reference, and the highest ratio is ~1.34 at 0°, which decreases to ~0.64 at 45°. Afterwards the value rises to ~1 at 90°.

The value of ϕ_2 corresponding to -30°, 0° and 30° also result in the same values on indentation modulus. Therefore, the angle ϕ_2 has only a small or even negligible effect on both the indentation modulus and the hardness ratio. It is confirmed that the angle Φ is the predominant factor affecting the anisotropic mechanical properties of the hexagonal Ti_2AlN material. The Φ angle is only considered in the comparison of the mechanical properties derived from experiments and calculation for the Ti_2AlN material.

3.3 Comparison of experimental and calculated results

In order to compare the results obtained experimentally with the calculation results, elastic modulus and hardness obtained from experiment and simulation are plotted as a function of angle Φ in Fig. 9, where the experimental hardness is normalized using a reference value of the hardness at Φ = 90°.

As shown in Fig. 9(a), the experimental indentation modulus exhibits the same trend as the one calculated using the Vlassak-Nix model. However, the elastic modulus values obtained by indentation, especially at Φ angles ranging from 50° to 90°, are lower than the data derived from the theoretical model. In the current work, the calculated experimental indentation modulus started from ~297 GPa for the basal plane and increased to ~303 GPa at 37°, then decreased to ~290 GPa for the prismatic plane. It is notable that the minimum value of the experimentally obtained indentation modulus is much lower than the one predicted by the Vlassak-Nix model, with a difference of about 18 %.

The hardness and the normalized hardness both show an initial decrease followed by an increase with an increasing angle, similar to that of the data derived from the easy-slip model (Fig. 9(b)). The maximum normalized experimental *H* ratio is around 1.24, being slightly lower than that of 1.34 derived from the easy-slip model, the general behaviors determined from experiment and calculation are comparable. The

easy-slip model yields a minimum value of ~0.64 at Φ of 45°, which is slightly lower than that from experiments at Φ of 43°. Due to the limitation of the easy-slip model, small differences between the hardness derived from the experiments and the prediction exist. In addition, no absolute value of hardness can be calculated and only relative values can be estimated.

Considering the uncertainty associated with the grain orientation within the selected areas and possibly a slight texture ($f(00l) = 0.07$) resulting from FAST/SPS procedure, experimental data in the Φ range from 0° to 30° are missing. The differences between the experimental and calculated values can result from different factors. First, the selection of different elastic constants of Ti_2AlN material based on those reported in the literature will result in different values obtained from calculation. Second, the assumption of active slip systems without the consideration of the less possible ones and unidirectional slip reduce the accuracy of the model predictions. In spite of this, the Vlassak-Nix model and easy-slip model allow for a very reasonable estimate of the elastic modulus and hardness of the hexagonal Ti_2AlN material, especially regarding the general tends, thus providing the feasibility for extending the investigation to other members of the MAX phase family.

Actually, in the current work, a minor effect of pile-up leading to slightly and leading to an increase indentation contact area, however, note that such any increase in contact area would lead actually to a decrease of the modulus, hence modulus values thus derived would be even lower, leading to even less agreement of experimental data and calculated curve. Moreover, regarding the experimental data, the modulus decrease with increasing angle above 30° whereas the hardness is rather constant above 30°, hence, any association of this behavior with pile-up is not reasonable, since both would be affected in a similar way and, in fact, the hardness even to a stronger extend since it is related to the contact area whereas the modulus is related to its square route.

On the other hand, regarding the calculated modulus values, the Vlassak-Nix model which derived the apparent to be measured value for indentation testing from the elastic parameter matrix, will be affected in the same way by any pile-up in different directions, since the area is integrated. Therefore, it will have the same uncertainty, if any since, however, consideration of pile-up by the model is not possible and hence in a comparison any effect related to pile-up will cancel. Regarding the hardness this only slightly different, since it is normalized using the easy-slip model. However, since the derivation as well as the experiment data do not consider pile-up, the effect should again cancel each other.

Considering all discussed above, the pile-up is negligible in the contact of this work, and the comparison of the values derived from experiments and modellings in the current work is reasonable.

4. Conclusions

The anisotropic mechanical properties of the layered Ti_2AlN MAX phase with a hexagonal structure was investigated for the first time via indentation mapping tests combined with EBSD characterization. The experimentally determined values of indentation modulus and hardness as a function of rotation angles of Ti_2AlN ceramic were rationalized, based on the Vlassak-Nix and easy-slip model, respectively.

While the mechanical properties of Ti_2AlN material are clearly anisotropic, indentation modulus and hardness do not follow the same trend. As expected, ϕ_2 has a negligible influence and Φ was the predominant factor for the anisotropy of the mechanical response. As Φ increased, the modulus increased in the range of 0° to 30° then decreased strongly, while the hardness decreased at first for 0° to 43° and increased slightly for higher angles. Based on the Vlassak-Nix and easy-slip models, it is shown that ϕ_2 has a negligible effect. For increasing Φ, the indentation modulus based on the Vlassak-Nix model increased at first and then decreased continuously, while the hardness ratio determined from the easy-slip model decreased to the minimum value at 45° and then increased slightly.

The general behaviors of the experimentally determined modulus and hardness are well estimated by the Vlassak-Nix and easy-slip model, respectively. The minimum modulus value at Φ = 90° (~290 GPa) is higher than that obtained experimentally (~239 GPa), but the maximum values for both experiment and simulation are almost the same. The differences between the experimental results and the calculated ones are likely related to the selection of elastic constants and the assumption of slip systems. Overall, this work demonstrates a promising methodology to investigate the mechanical properties of the novel and highly anisotropic MAX phase materials, and also further provides a guideline for the design and development of the MAX phase materials in various application fields.

Acknowledgements

The authors would like to thank Dr. E. Wessel, Dr. D. Grüner, Mr. M. Ziegner and Mr. J. Borowec and for providing the SEM, EBSD, XRD and AFM data. Supports from Prof. L. Singheiser and Prof. M. Krüger are highly acknowledged. Xiaoqiang Li and Gang Yan gratefully acknowledge the support from the China Scholarship Council (CSC) of China. Prof. J. Gonzalez-Julian acknowledges the financial support by the Germany's Federal Ministry of Education and Research ("Bundesministerium für Bildung und Forschung") under the MAXCOM project (03SF0534).

References

[1] M.W. Barsoum, The $M_{n+1}AX_n$ phases: a new class of solids; thermo-dynamically stable nanolaminates, Prog. Solid. State. Chem. 28 (2000) 201-281.

[2] Y. Bai, N. Srikanth, C.K. Chua, K. Zhou, K, Density Functional Theory Study of $M_{n+1}AX_n$ Phases: A Review, Crit. Rev. Solid. State. (2017) 1-51.

[3] M.W. Barsoum, M. Radovic, Elastic and Mechanical Properties of the MAX Phases, Annu. Rev. Mater. Res. 41 (2011) 195-227.

[4] Z.M. Sun, Progress in research and development on MAX phases: a family of layered ternary compounds, Int. Mater. Rev. 56 (2011) 143-166.

[5] M. Undberg, K. Lindgren, T. El-Raghy, G. Malmqvist, US Patent 10, (2004) 544, 467.

[6] T. El-Raghy, M.W. Barsoum, US Patent 10, (2003) 666, 639.

[7] H. Hashimoto, Z.M. Sun, An approach to the synthesis of AlN-Ti_2AlN composite, J. Jpn. Soc. Powder. Metall. 56 (2009) 541-5.

[8] S. Lu, X.Q. Li, Y.F. Zhou, W.T. Xu, W. Pan, Synthesis and mechanical properties of TiB_2/Ti_2AlN composites fabricated by hot pressing sintering, J. Ceram. Soc. Jan. 126 (11) (2018) 900-905.

[9] C. Salvo, E. Chicardi, C. García-Garrido, J.A. Jiménez, C. Aguilar, J. Usuba, R.V. Mangalaraja, The influence of mechanical activation process on the microstructure and mechanical properties of bulk Ti_2AlN MAX phase obtained by reactive hot pressing, Ceram. Int. 45 (14) (2019) 17793-17799.

[10] I.M. Lowa, W.K. Pang, S.J. Kennedy, R.I. Smith, High-temperature thermal stability of Ti_2AlN and Ti_4AlN_3: A comparative diffraction study, J. Eur. Ceram. Soc. 31 (2011) 159-166.

[11] M. Yan, Y.L. Chen, B.C. Mei, Synthesis of high purity Ti_2AlN ceramic by hot pressing, Trans. Nonferrous. Met. Soc. China. 18 (1) (2008) 82-5.

[12] X.Q. Li, J. Gonzalez-Julian, J. Malzbender, Fabrication and mechanical performance of Ti_2AlNprepared by FAST/SPS, J. Eur. Ceram. Soc. 40 (2020) 4445–4453.

[13] Z.J. Lin, M.J. Zhuo, M.S. Li, J.Y. Wang, Y.C. Zhou, Synthesis and microstructure of layered-ternary Ti_2AlN ceramic, Scr. Mater. 56 (2007) 1115-1118.

[14] Y. Liu, Z.Q. Shi, J.P Wang, G.J Qiao, Z.H Jin, Z.J Shen, Reactive consolidation of layered-ternary Ti_2AlN ceramics by spark plasma sintering of a Ti/AlN powder mixture, J. Eur. Ceram. Soc. 31 (2011) 863-868.

[15] A. Guitton, A. Joulain, L. Thilly, C. Tromas, Dislocation analysis of Ti_2AlN deformed at room temperature under confining pressure, Philos. Mag. 92 (36) (2012) 4536-4546.

[16] J.L. Jordan, N.N. Thadhani, Effect of shock-activation on post-shock reaction synthesis of ternary ceramics, AIP conference proceedings, IOP Institute of Physics Publishing Ltd. (2) (2002) 1097-1100.

[17] W.L. Liu, C.J. Qiu, J. Zhou, Z.H. Ding, X.B Zhou, S.Y. Du, Y.H. Han, Q. Huang, Fabrication of Ti_2AlN ceramics with orientation growth behavior by the microwave sintering method, J. Eur. Ceram. Soc. 35 (5) (2015) 1385-1391.

[18] T. Ouisse, E. Sarigiannidou, O. Chaix-Pluchery, H. Roussel, B. Doisneau, D. Chaussende, High temperature solution growth and characterization of Cr_2AlC single crystals, J. Cryst. Growth. 384 (2013) 88-95.

[19] M. Magnuson, M. Mattesini, N.V. Nong, P. Eklund, L. Hultman, Electronic-structure origin of the anisotropic thermopower of nanolaminated Ti_3SiC_2 determined by polarized x-ray spectroscopy and Seebeck measurements, Phys. Rev. B 85 (2012) 195134.

[20] V. Mauchamp, W. Yu, L. Gence, L. Piraux, T. Cabioc'h, V. Gauthier, P. Eklund, S. Dubois, Anisotropy of the resistivity and charge-carrier sign in nanolaminated Ti_2AlC: Experiment and ab initio calculations, Phys. Rev. B 87 (2013) 235105.

[21] T. Joelsson, A. Flink, J. Birch, and L. Hultman, Deposition of single-crystal Ti_2AlN thin films by reactive magnetron sputtering from a 2Ti:Al compound target, J. Appl. Phys. 102 (2007) 074918.

[22] J. Etzkorn, M. Ade, H. Hillebrecht, Ta_3AlC_2 and Ta_4AlC_3 Single-Crystal Investigations of Two New Ternary Carbides of Tantalum Synthesized by the Molten Metal Technique, Inorg. Chem. 46 (2007) 1410-1418.

[23] F. Mercier, T. Ouisse, D. Chaussende, Morphological instabilities induced by foreign particles and Ehrlich-Schwoebel effect during the two-dimensional growth of crystalline Ti_3SiC_2, Phys. Rev. B 83 (2011) 075411.

[24] F. Mercier, O. Chaix-Pluchery, T. Ouisse, D. Chaussende, Raman scattering from Ti_3SiC_2 single crystals, Appl. Phys. Lett. 98 (8) (2011) 081912-3.

[25] A. Murugaiah, A. Souchet, T. El-Raghy, M. Radovic, M. Sundberg, M.W. Barsoum, Tape Casting, Pressureless Sintering, and Grain Growth in Ti_3SiC_2 Compacts, J. Am. Ceram. Soc. 87 (2004) 550-556.

[26] C.F. Hu, Y. Sakka, H. Tanaka, T. Nishimura, S. Grasso, Fabrication of Textured Nb_4AlC_3 Ceramic by Slip Casting in a Strong Magnetic Field and Spark Plasma Sintering, J. Am. Ceram. Soc. 94 (2011) 410-415.

[27] C.F. Hu, Y. Sakka, T. Nishimura, S.Q. Guo, S. Grasso, H. Tanaka, Physical and mechanical properties of highly textured polycrystalline Nb_4AlC_3 ceramic, Sci. Technol. Adv. Mater. 12 (2011) 044603.

[28] C.F. Hu, Y. Sakka, S. Grasso, T. Nishimura, S.Q. Guo, H. Tanaka, Shell-like nanolayered Nb_4AlC_3 ceramic with high strength and toughness, Scr. Mater. 64 (2011) 765-768.

[29] T. Lapauw, K. Vanmeensel, K. Lambrinou, J. Vleugels, A new method to texture dense $M_{n+1}AX_n$ ceramics by spark plasma deformation, Scr. Mater. 111 (2016) 98-101.

[30] X.Q. Li, X. Xie, J. Gonzalez-Julian, J. Malzbender, R.Yang, Mechanical and oxidation behavior of textured Ti_2AlC and Ti_3AlC_2 MAX phase materials, J. Eur. Ceram. Soc, 40 (2020) 5258-5271.

[31] Y. Liu, Y.X. Li, F. Li, H. Cui, Y.P Pu, S.W. Guo, Z.Q. Shi, Highly textured Ti_2AlN ceramic prepared via thermal explosion followed by edge-free spark plasma sintering, Scr. Mater. 136 (2017) 55-58.

[32] X. Duan, L. Shen, D. Jia, Y. Zhou, S. van der Zwaag, W.G. Sloof, Synthesis of high-purity, isotropic or textured Cr_2AlC bulk ceramics by spark plasma sintering of pressure-less sintered powders, J. Eur. Ceram. Soc. 35 (2015) 1393-1400

[33] C. Brüsewitz, I. Knorr, H. Hofsäss, M.W. Barsoum, C.A. Volkert, Single crystal pillar microcompression tests of the MAX phases Ti_2InC and Ti_4AlN_3, Scr. Mater. 69 (2013) 303-306.

[34] Y. Kabiri, N. Schrenker, J. Müller, M. Mačković, E. Spiecker, Direct observation of dislocation formation and plastic anisotropy in Nb_2AlC MAX phase using in situ nanomechanics in transmission electron microscopy, Scr. Mater. 137 (2017) 104-108.

[35] M. Higashi, S. Momono, K. Kishida, N.L.Okamoto, H. Inui, Anisotropic plastic deformation of single crystals of the MAX phase compound Ti_3SiC_2 investigated by micropillar compression, Acta. Mater. 161 (2018) 161-170.

[36] W.C. Oliver, G.M. Pharr, An Improved Technique for Determining Hardness and Elastic-Modulus Using Load and Displacement Sensing Indentation Experiments, J. Mater. Res. 7 (6) (1992) 1564-1583.

[37] J. Malzbender, G. de With, The use of the indentation loading curve to detect fracture of coatings, Surf. Coat. Technol. 137 (1) (2001) 72-76

[38] J. Malzbender, G. de With, The use of the loading curve to assess soft coatings, Surf. Coat. Technol. 127 (2-3) (2000) 265-272

[39] A.N. Wang, J.F. Nonemacher, G. Yan, M. Finsterbusch, J. Malzbender, M. Krüger, Mechanical properties of the solid electrolyte Al-substituted $Li_7La_3Zr_2O_{12}$(LLZO) by utilizing micro-pillar indentation splitting test, J. Eur. Ceram. Soc. 38 (2018) 3201-3209.

[40] J.F. Nonemacher, C. Hüter, H. Zheng, J. Malzbender, M. Krüger, R. Spatschek, M. Finsterbusch, Microstructure and properties investigation of garnet structured $Li_7La_3Zr_2O_{12}$ as electrolyte for all-solid-state batteries, Solid. State. Ion. 321 (2018) 126-134.

[41] J.J. Vlassak, W. Nix, Measuring the elastic properties of anisotropic materials by means of indentation experiments, J. Mech. Phys. Solids. 42 (8) (1994) 1223-1245.

[42] A. Staroselskya, L. Anand, A constitutive model for hcp materials deforming by slip and twinning: application to magnesium alloy AZ31B, Int. J. Plast. 19 (2003) 1843-1864.

[43] D. Catoor, Y.F. Gao, J. Geng, M.J.N.V. Prasad, E.G. Herbert, K.S. Kumar, G.M. Pharr, E.P. George, Incipient plasticity and deformation mechanisms in single-crystal Mg during spherical nanoindentation, Acta. Mater. 61 (2013) 2953-2965.

[44] J. Kwon, M.C. Brandes, P. Sudharshan Phani, A.P. Pilchak, Y.F. Gao, E.P. George, G.M. Pharr, M.J. Mills, Characterization of deformation anisotropies in an α-Ti alloy by nanoindentation and electron microscopy, Acta. Mater. 61 (2013) 4743-4756.

[45] A. Datye, L. Li, W. Zhang, Y.J. Wei , Y.F. Gao, G.M. Pharr, Extraction of Anisotropic Mechanical Properties From Nanoindentation of SiC-6H Single Crystals, J. Appl. Mech. 83 (2016) 091003-1.

[46] Q. Chen, F. Gao, T. Csanádi, J. Xu, M.S. Fu, M. Wang, J. Dusza, Investigation of anisotropic mechanical properties of textured $KSr_2Nb_5O_{15}$ ceramics via ab-initio calculation and nanoindentation, J. Am. Ceram. Soc. 101 (2018) 5138–5150.

[47] P. Haušild, A. Materna, J. Nohava, Characterization of Anisotropy in Hardness and Indentation Modulus by Nanoindentation. Metallogr. Microstruct. Anal. 3 (2014) 5-10.

[48] T. Csanádi, S. Grasso, A. Kovalčíková, J. Dusza, M. Reece, Nanohardness and elastic anisotropy of ZrB_2 crystals, J. Eur. Ceram. Soc. 36 (2016) 239–242.

[49] J.B. Jr. Wachtman, W. Tefft, D.G. Jr. Lam, R.P. Stinchfield, Elastic Constants of Synthetic Single-Crystal Corundum at Room Temperature, J. Am. Ceram. Soc. 43 (6) (1960) 334-334.

[50] G. Yan, S. Yu, W. Yang, X. Li, H. Tempel, H. Kungl, J. Malzbender, Anisotropy of the mechanical properties of $Li_{1.3}Al_{0.3}Ti_{1.7}(PO_4)_3$ solid electrolyte material, J. Power. Sources. 437 (2019) 226940.

[51] T. Csanádi, M. Bl'anda, N.Q. Chinh, P. Hvizdoš, J. Dusza, Orientation-dependent hardness and nanoindentation-induced deformation mechanisms of WC crystals, Acta. Mater. 83 (2015) 397-407.

[52] T. Csanádi, D. Németh, J. Dusza, Z. Lenčéš, P. Šajgalík, Nanoindentation induced deformation anisotropy in β-Si_3N_4 ceramic crystals, J. Eur. Ceram. Soc. 36 (12) (2016) 3059-3066.

[53] ASTM International. ASTM E2546-07 Standard Practice for Instrumented Indentation Testing. West Conshohocken, PA; ASTM International, 2007.

[54] D. Mainprice, R. Hielscher, H. Schaeben, Calculating anisotropic physical properties from texture data using the MTEX open-source package, Geological Society, London, Special Publications 360 (1) (2011) 175-192.

[55] T. Csanádi, D. Németh, C. Zhang, J. Dusza, Nanoindentation derived elastic constants of carbon fibres and their nanostructural based predictions, Carbon 119 (2017) 314-325

[56] Y. Hu, X. Zhao, J.J. Vlassak, Z. Suo, Using indentation to characterize the poroelasticity of gels, Appl. Phys. Lett. 96 (12) (2010) 121904.

[57] J. Vlassak, M. Ciavarella, J. Barber, X. Wang, The indentation modulus of elastically anisotropic materials for indenters of arbitrary shape, J. Mech. Phys. Solids. 51 (9) (2003) 1701-1721.

[58] T. El-Raghy, A. Zavaliangos, M.W. Barsoum, S.R. Kalidindi, Damage mechanisms around hardness indentations in Ti_3SiC_2, J. Am. Ceram. Soc. 80 (1997) 513-516.

[59] L. Farber, M.W. Barsoum, A. Zavaliangos, T. El-Raghy, Dislocations and stacking faults in Ti_3SiC_2, J. Am. Ceram. Soc. 81 (1998) 1677-1681.

[60] M.W. Barsoum, L. Farber, T. El-Raghy, Dislocations, kink bands, and room temperature plasticity of Ti_3SiC_2, Metall. Mater. Trans. 30 (1999) 1727-1738.

[61] Z.M. Sun, Z.F. Zhang, H. Hashimoto, T. Abe, Ternary compound Ti_3SiC_2: Part II. Deformation and fracture behavior at different temperatures, Mater. Trans. 43 (2002) 432-435.

[62] B.J. Kooi, R.J. Poppen, N.J.M. Carvalho, J.ThM. De Hosson, M.W. Barsoum, Ti_3SiC_2: a damage tolerant ceramic studied with nano-indentations and transmission electron microscopy, Acta. Mater. 51 (2003) 2859-2872.

[63] J.M. Molina-Aldareguia, J. Emmerlich, J.P. Palmquist, U. Jansson, L. Hultman, Kink formation around indents in laminated Ti_3SiC_2 thin films studied in the nanoscale, Scr. Mater. 49 (2003) 155-160.

[64] A. Guitton, A. Joulain, L. Thilly, C. Tromas, Dislocation analysis of Ti_2AlN deformed at room temperature under confining pressure, Philos. Mag. A 92 (2012) 4536-4546.

[65] E. Schmid, W. Boas, Plasticity of Crystals, F.A. Hughes & Co. Ltd., London, (1950).

[66] R.W.K. Honeycombe, The Plastic Deformation of Metals, Edward Arnold Publishers Ltd., London, 1968.

[67] A. Bouhemadou, R. Khenata, M. Chegaar, Structural and elastic properties of Zr_2AlX and Ti_2AlX (X = C and N) under pressure effect, Eur. Phys. J. B 56 (2007) 209–215.

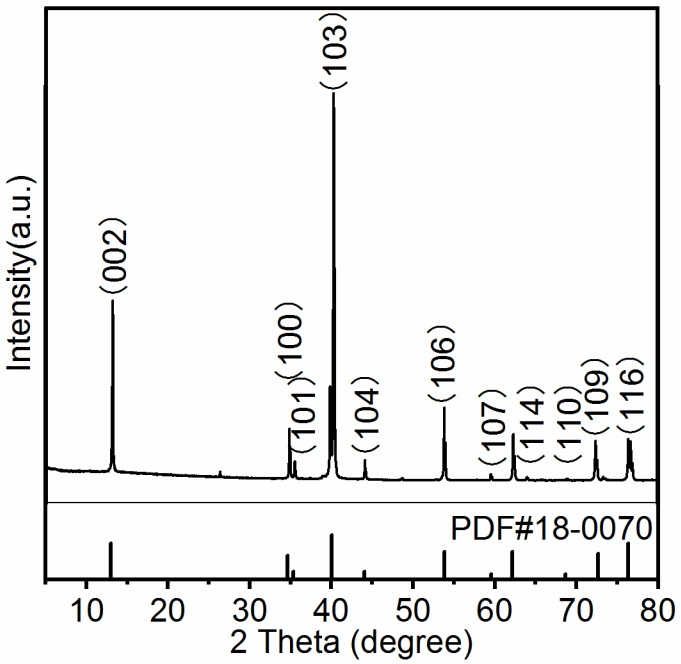

Fig. 1. XRD scan of Ti_2AlN specimen.

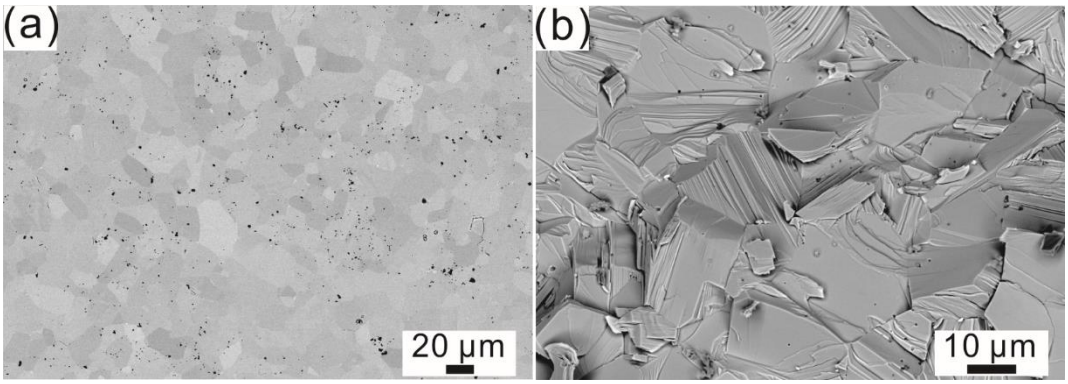

Fig. 2. SEM images of Ti_2AlN specimen: (a) polished surface, and (b) fracture surface.

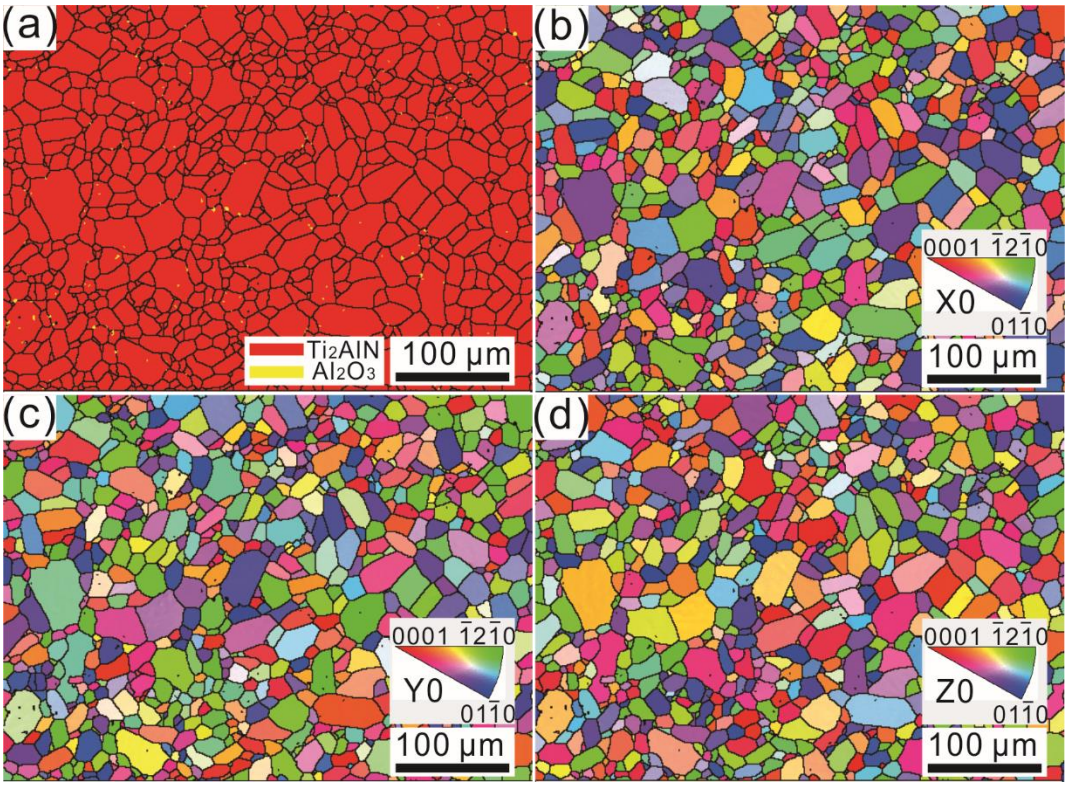

Fig. 3. (a) Phase map and the inverse pole figure maps of the Ti_2AlN samples determined from EBSD with respect to (b) X0, (c) Y0, and (d) Z0.

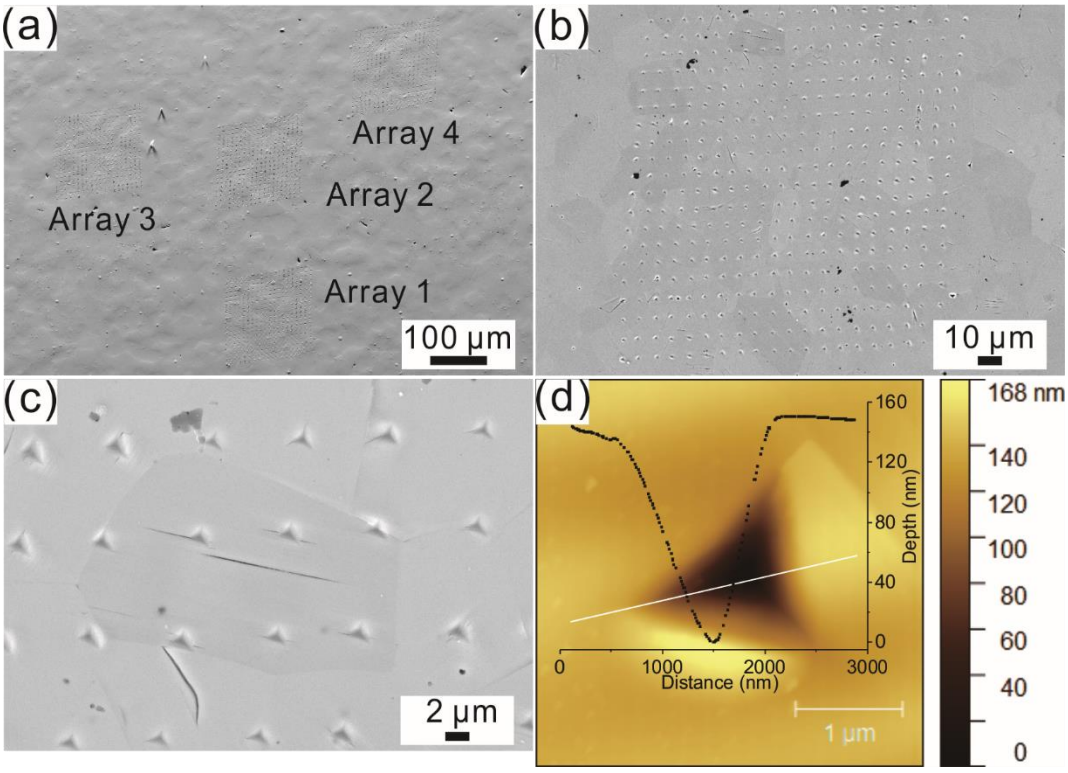

Fig. 4. SEM images of (a) the selected areas, (b) a typical indentation array (Array 3), (c) representative imprints and (d) AFM image of the imprint after nanoindentation.

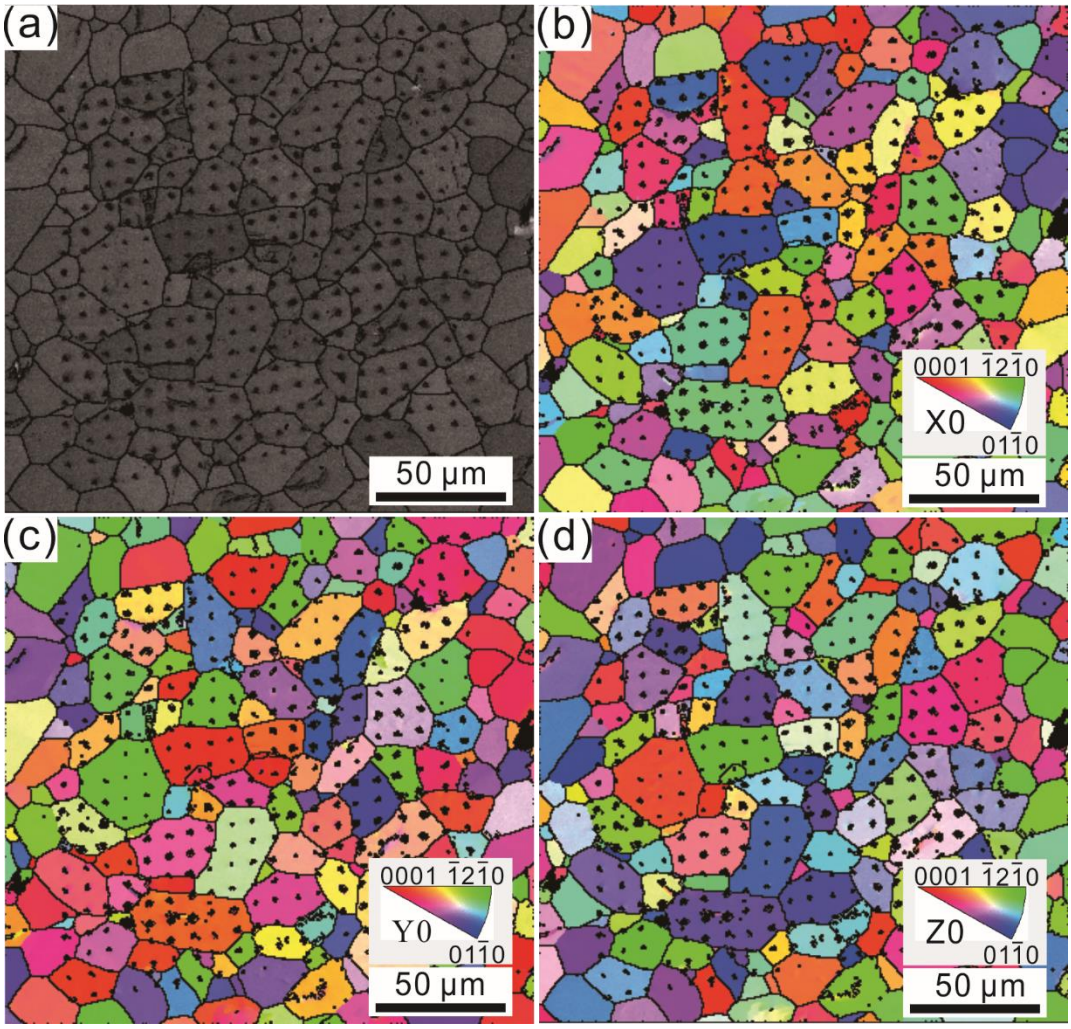

Fig. 5. (a) EBSD band contrast and grain boundaries image and the inverse pole figure orientation maps with respect to (b) X0, (c) Y0, (d) Z0 of array 3.

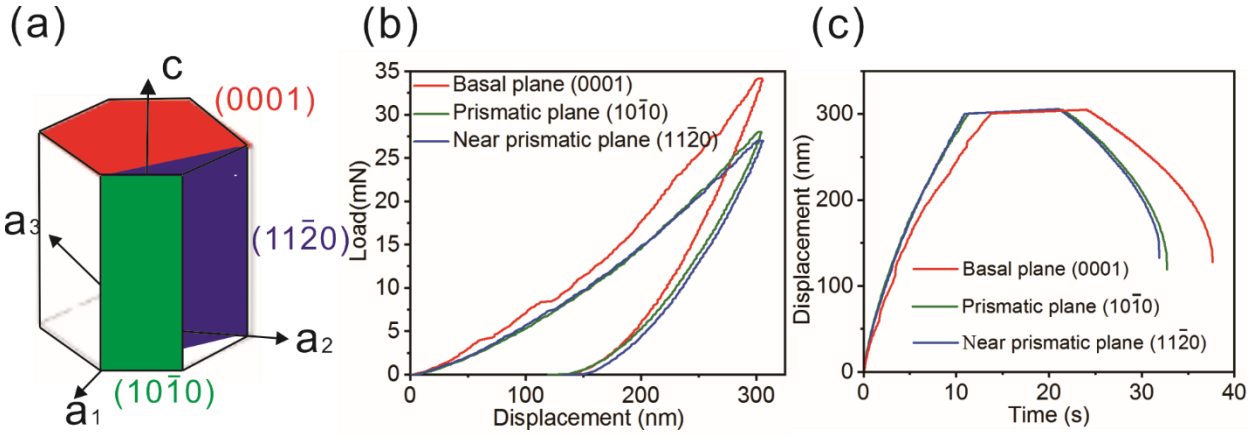

Fig. 6. (a) Schematic of the three planes within a hexagonal crystal indented, (b) corresponding representative load-displacement curves and (c) the curve of displacement as a function of time for indentation performed on specified basal plane and prismatic planes.

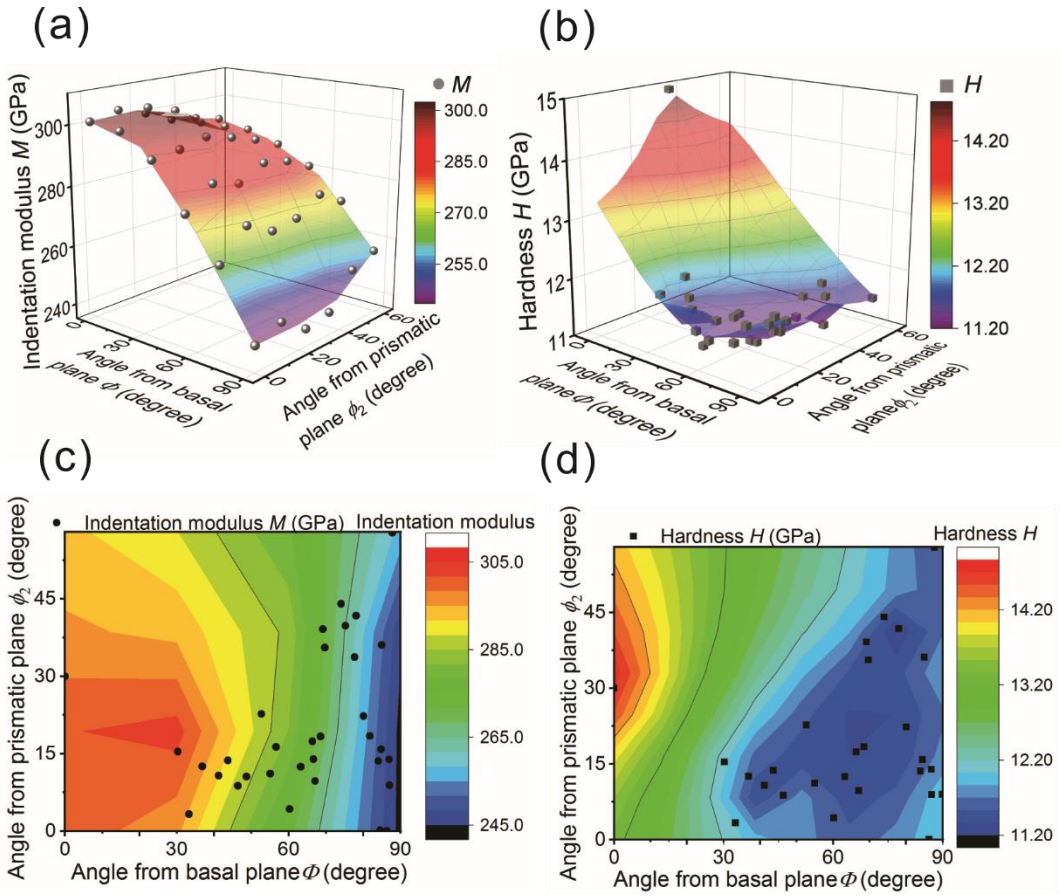

Fig. 7. Experimentally determined (a) indentation modulus and (b) hardness of the Ti_2AlN as a function of the angles from the basal (Φ) and prismatic planes (ϕ_2). The surface maps are applied to visualize the dependency of mechanical properties on the angles from the basal (Φ) and prismatic planes (ϕ_2). And corresponding 2D color-map of the experimentally determined (c)

indentation modulus and (d) hardness of the Ti_2AlN as a function of the angles from the basal (Φ) and prismatic planes (ϕ_2).

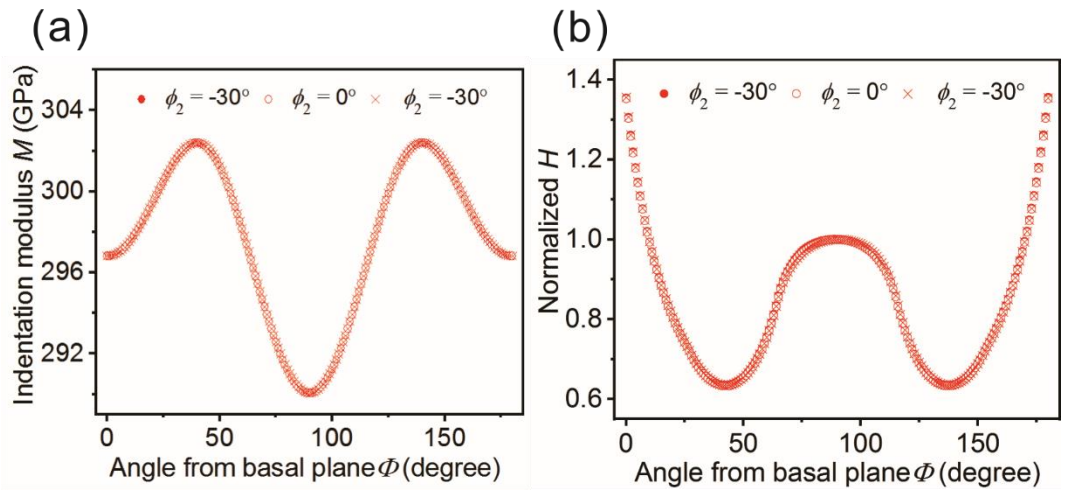

Fig. 8. The (a) indentation modulus and (b) hardness ratio (normalized H) determined from simulation as a function of the angle from the basal plane, Φ. Representative angles ϕ_2 of -30°, 0° and 30° are indicated here to show its impact on the mechanical properties.

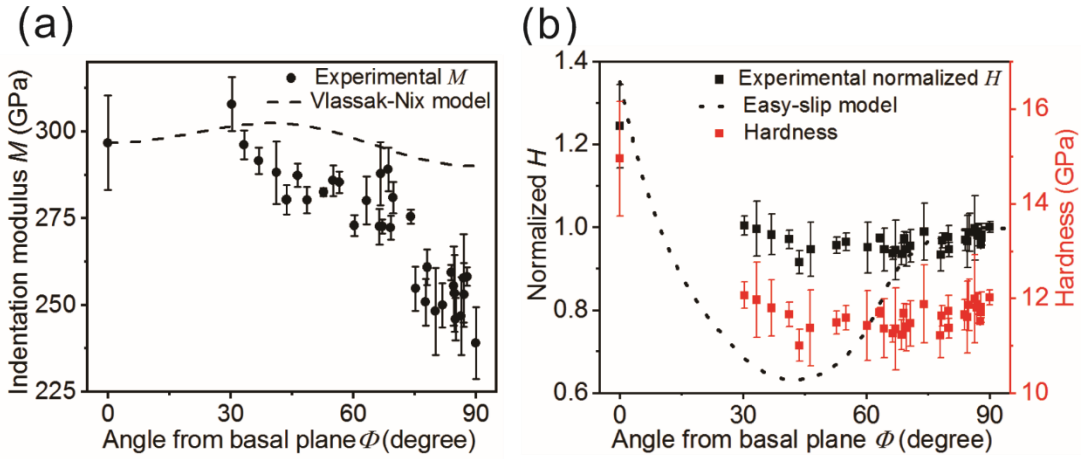

Fig. 9. (a) Indentation modulus and (b) hardness of Ti_2AlN grains obtained from experiment and simulation as a function of the angle from the basal plane, Φ.

Table 1 Characteristic parameters of the as-obtained Ti_2AlN material.

Ti_2AlN	Lattice parameters							Amount 1** (wt. %)	Amount 2*** (vol. %)	
	Space	a*	b*	c* (Å)	α	β	γ	Ti_2AlN	Ti_2AlN	Al_2O_3
	P63/m	2.98	2.98	13.64	90	90	12	~100	99.7	0.3

*The lattice parameters were characterized via XRD using Rietveld refinement.

**The amount 1 is the purity obtained via XRD using Rietveld refinement.

***The amount 2 refers to the purity obtained via EBSD technique.